A dual S-scheme heterojunction SrTiO₃/SrCO₃/C-doped TiO₂ as H₂ production photocatalyst and its charge transfer mechanism

Jing Wang [a], Qi Hao [a], Rongzhong Yang [a], Xingyu Niu [a], Rui Wang [a], Liping Yang [c], Qinghong Huang [a], Jilei Ye [a,*], Huiying Yang [c,*], Yuping Wu [a,b,**]

[a] School of Energy Science and Engineering, Nanjing Tech University, Nanjing, Jiangsu 211816, China
[b] School of Energy and Environment, South East University, Nanjing, Jiangsu 211189, China
[c] Pillar of Engineering Product Development, Singapore University of Technology and Design, 487372, Singapore

ARTICLE INFO

ABSTRACT

Constructing an S-scheme heterojunction is a highly effective approach for enhancing photocatalytic performance. However, the impact of a single S-scheme heterojunction on charge transfer is limited. To overcome this constraint, a dual S-scheme heterojunction, SrTiO₃/SrCO₃/C-doped TiO₂ (referred to as ST/SC/CT), is designed for UV-vis-driven hydrogen production. The mass-normalized and effective surface area-normalized hydrogen production activities of ST/SC/CT are higher than those of ST and CT, respectively. The enhancement in photocatalytic performance is primarily attributed to the improved separation and transfer of photogenerated charge carriers by the dual S-scheme heterojunction. Moreover, C-doping effectively extends the light absorption range from UV to visible and greatly improves the absorption intensity. The heterojunction and charge transfer mechanism are also investigated through microscopy and spectroscopic techniques, as well as density functional theory (DFT) calculations. This work offers valuable insights for the design of novel composites by combining surface modification with heterojunction engineering.

1. Introduction

Photocatalytic hydrogen production is an effective solution to alleviate the increasing global energy and environmental challenges. Since the pioneering work about the water splitting on TiO₂ photoelectrode in 1972 [1], various semiconductor materials have been extensively investigated as photocatalysts for hydrogen generation from water splitting, such as TiO₂ [2–5], CdS [6–8], ZnIn₂S₄ [9–11], SrTiO₃ [12–14], etc. Among them, SrTiO₃, as a representative oxide, has emerged as an important material for photocatalytic hydrogen production due to its non-toxicity, cost-effectiveness, ease of synthesis, high response to ultraviolet light, and eco-friendliness [15]. But the limited absorption of visible light and the high recombination rate of photo-generated charge carriers significantly restrict the photocatalytic hydrogen production performance of SrTiO₃ [16]. An efficient strategy to overcome the above drawbacks is to enhance light absorption and facilitate the separation of charge carrier by forming a heterojunction with other semiconductors[17–20].

TiO₂ has a staggered band alignment with SrTiO₃, and it exhibits excellent stability and photocatalytic hydrogen production activity, so it is an ideal candidate material for constructing a heterojunction with SrTiO₃ [21–24]. The inability to absorb visible light is still the main drawback hindering the application of TiO₂. To overcome this limitation, carbon doping is employed as a promising approach to enhance the visible light absorption capability of TiO₂ photocatalysts, consequently improving their photocatalytic performance [25–29]. Therefore, it is a good strategy to combine carbon-doped TiO₂ with SrTiO₃ to form a heterojunction to synergistically improve light absorption and charge separation efficiency, consequently improving photocatalytic hydrogen evolution activity.

Recently, step-scheme (S-scheme) heterojunction photocatalysts composed of a reduction photocatalyst (RP) and an oxidation photocatalyst (OP) have garnered significant attention due to their excellent ability to efficiently separate charge carriers and exhibit strong redox capabilities [30–33]. However, the interface between RP and OP in an S-scheme heterojunction often leads to high contact resistance and slow

---

carrier transfer. As a result, a dual S-scheme heterojunction with reduced contact resistance is emerging [34–36]. Importantly, the dual S-scheme heterojunction photocatalyst offers additional charge transfer pathways, leveraging the synergistic effect of multiple components to further enhance the separation of charge carriers. However, the insufficient interfacial contact among the three different catalysts in the dual S-scheme heterojunction and the unclear mechanism of long-term carrier transfer still present significant challenges.

In our work, we in situ construct $SrTiO_3/SrCO_3$ spheres modified C-doped TiO_2 sheets (abbreviated as ST/SC/CT) for hydrogen production by a simple solvothermal method. In addition, in situ nucleation, crystallization, and growth of $SrTiO_3$ (ST)/$SrCO_3$ (SC) occur on the surface of C-doped TiO_2 (CT), forming a dual S-scheme heterojunction, which effectively promotes the transfer of photogenerated charge carriers. $SrTiO_3$ and $SrCO_3$ share the same Sr source, nucleation sites, and matched band structures, resulting in lower contact potential barriers and effectively avoiding excessive lattice matching differences. Additionally, MXene acts as a nucleation substrate for $SrTiO_3/SrCO_3$ and a precursor for C-doped TiO_2, promoting intimate contact between $SrTiO_3/SrCO_3$ and C-doped TiO_2 over a large area. The UV-visible-driven hydrogen evolution reaction rate of ST/SC/CT is 1.893 and 5.033 times of ST and CT, respectively. Moreover, the charge transfer mechanism was confirmed as a dual S-scheme heterojunction through a combination of band structure experiments, internal electric field strength calculations, density functional theory (DFT) calculations on work function, and charge differential density distribution, alongside Kelvin probe force microscopy (KPFM). This work provides perspective for constructing high-performance S-scheme photocatalysts with charge transfer characteristics.

2. Experimental section

2.1. Preparation of ST/SC/CT

Firstly, 10 mmol of $Ti(OC_4H_9)_4$ and 2.116 g of $Sr(NO_3)_2$ were mixed with 20 mL of ethylene glycol. The resulting mixture was stirred for 15 min. Secondly, 10 mL of NaOH aqueous solution (5 mol/L) was added to create ST precursor solution. Thirdly, MXene dispersion was added into the ST precursor solution. Subsequently, the mixed solution was transferred into a 100 mL Teflon-lined stainless steel autoclave for a solvothermal treatment at 200 °C for 14 h. Then the precipitation was washed with deionized water and ethanol for several times, and put into a vacuum drying oven overnight. The product was ST/SC/CT.

Under the same solvothermal processes, the sample obtained without $Sr(NO_3)_2$ and $Ti(OC_4H_9)_4$ was labeled as CT, while the sample obtained without MXene was labeled as ST. In addition, the mass ratios of MXene to (MXene + ST) were 1 %, 5 %, 10 %, and 15 %, and the according samples were denoted as ST/SC/CT-1, ST/SC/CT-5, ST/SC/CT-10, and ST/SC/CT-15, respectively. The preparation conditions for all samples are shown in Table S1.

2.2. Characterization

The X-ray diffractometer (XRD) patterns of the samples were obtained using a BRUKER AXS GMBH (D8ADVANCE) instrument with Cu-Kα radiation, covering a 2θ range of 10°-90°. Scanning electron microscope (SEM) images were captured on Quanta200 scanning electron microscope. Transmission electron microscopy (TEM) images were acquired using a JEOL JEM-2100. The Raman spectra were obtained using a Raman microscope (LABRAM-HR, JY Co.). XPS measurements were conducted on a Thermofisher escalab 250xi spectrometer. UV-Visible diffuse reflectance spectra were recorded with an ultraviolet-visible spectrophotometer (UV 2600, Shimadzu Co.). Nitrogen adsorption and desorption measurements were carried out with an Autosorb iQ instrument, and surface areas were calculated using the Brunauer-Emmett-Teller (BET) method. Photoluminescence (PL) spectra were collected

by means of an Edinburgh spectrofluorometer (FLS980) with an excitation wavelength of 350 nm and a testing wavelength range of 380 nm to 600 nm. Atomic force microscopy (AFM) images and Kelvin probe force microscopy (KPFM) measurements were carried out using Bruker Multimode 8. Electron paramagnetic resonance (EPR) was performed on an ESR spectrometer (MEX-nano, Bruker) with a modulation frequency of 100 kHz and a microwave power of 15 mW.

2.3. Photocatalytic hydrogen evolution tests

The photocatalytic hydrogen evolution test was conducted using an all-glass automatic on-line trace gas analysis system (Labsolar-6A, Beijing PerfectLight). A 300 W Xe lamp is a UV-visible light source. The irradiation light density is 160 mW cm^{-2}. For each typical test, 20 mg of the photocatalyst was dispersed in 80 mL of aqueous solution containing triethanolamine (TEOA) sacrificial agent (8 mL of TEOA and 72 mL of deionized water). Prior to UV-visible light irradiation, it was important to completely degas the dissolved air in the mixed solution through the evacuation system. To maintain the photocatalytic reaction temperature at 6 °C, an ethanol circulating liquid trap system was employed. Finally, the online TCD system with a gas chromatograph (FULI 979011) was used to calibrate the hydrogen evolution.

2.4. Electrochemical measurements

The transient photocurrent response (I-t), cyclic voltammetry (CV), linear sweep voltammetry (LSV), and electrochemical impedance (EIS) of the photocatalyst were measured using a three-electrode device (CHI 660D potentiostat) with a constant potentiometer. The working electrode, reference electrode (saturated calomel electrode), and counter electrode (Pt electrode) were used for the experiments. Fluorine-doped tin oxide (FTO) glasses were cleaned before preparing the working electrode, which was coated with a slurry of sample (5 mg) in ethanol (1 mL) containing Nafion (5 %). The area of the working electrode was 1 cm^2. The electrolyte used was Na_2SO_4 solution (0.2 M) purified with nitrogen gas. A 300 W Xe lamp served as the light source for the experiment.

2.5. Density functional theory (DFT) calculations

The first principle calculations are performed by Vienna Ab initio Simulation Package(VASP) [37] with the projector augmented wave (PAW) method [38]. The exchange-functional is treated using the Perdew-Burke-Ernzerhof (PBE) [37] functional, in combination with the DFT-D3 correction [39]. The cut-off energy of the plane-wave basis is set at 450 eV. For the optimization of both geometry and lattice size, the Brillouin zone integration is performed with 1*1*1 Monkhorts-Pack [40] kpoint sampling. The self-consistent calculations apply a convergence energy threshold of 105 eV. The equilibrium geometries and lattice constances are optimized with maximum stress on each atom within 0.02 eV/Å.

3. Results and discussion

The synthesis scheme of ST/SC/CT photocatalyst is illustrated in Fig. 1a. $Ti(OC_4H_9)_4$, $Sr(NO_3)_2$, and ethylene glycol were employed as the titanium precursor, strontium source, and structure-directing agent, respectively. NaOH plays a crucial role in maintaining an alkaline environment. Subsequently, the MXene sheets are dispersed in the alkaline precursor solution of ST. The reaction between the functional groups on the surface of the MXene sheets and the hydrogen ions in water molecules leads to the deprotonation of the hydroxyl groups, resulting in a negative charge on the MXene surface. On one hand, Sr^{2+} is preferentially adsorbed to the surface of MXene through electrostatic adsorption and reacts with NaOH, resulting in the formation of $Sr(OH)_2$ (Eq. 1). The functional groups on the MXene surface play a role in
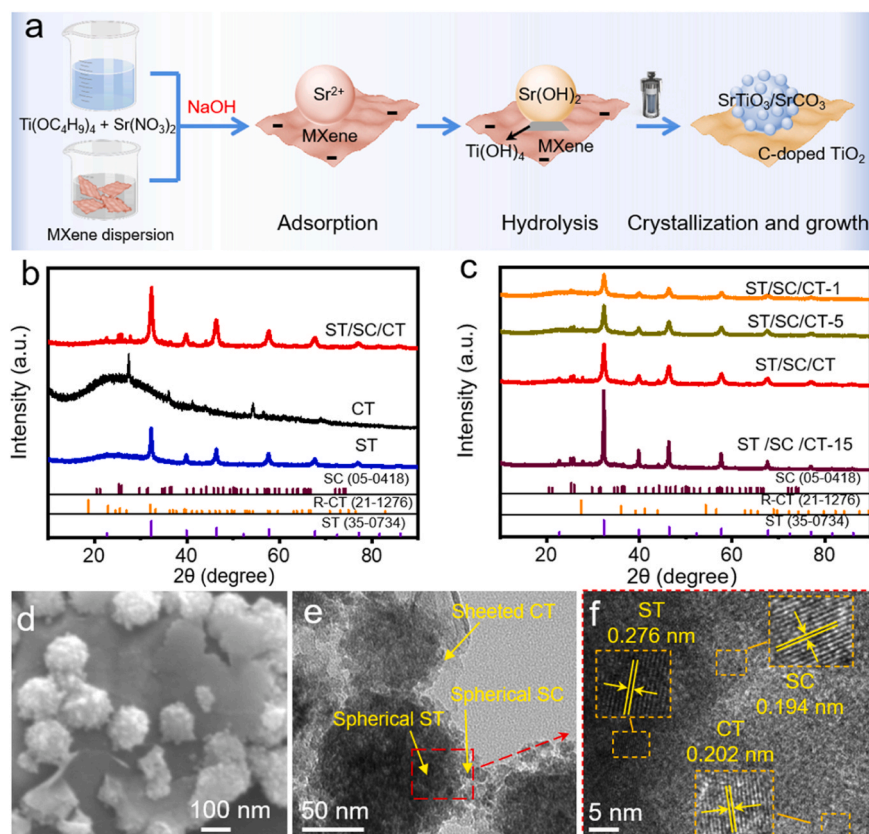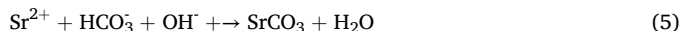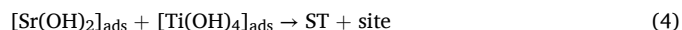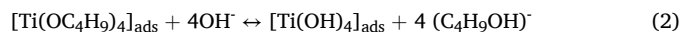
Fig. 1. Synthesis scheme, structure, and morphology characterization. (a) Synthesis scheme of the ST/SC/CT photocatalyst. (b) XRD patterns of ST, CT, and ST/SC/CT. (c) XRD patterns of various samples. For ST/SC/CT-1, ST/SC/CT-5, ST/SC/CT, and ST/SC/CT-15, the mass ratios of MXene to (ST+MXene) are 1%, 5%, 10%, and 15%, respectively. (d) SEM, TEM, and HRTEM images of ST/SC/CT, respectively.

pinning $Sr(OH)_2$, facilitating the dispersion and preventing excessive agglomeration. On the other hand, due to the surface tension at the liquid-solid interface, $Ti(OC_4H_9)_4$ tends to accumulate at the contact corner between $Sr(OH)_2$ and MXene, and undergoes the hydrolysis reaction (Eq. 2) to generate $Ti(OH)_4$. Consequently, the resultant $Ti(OH)_4$ further bridges $Sr(OH)_2$ and MXene, thus enhancing the interfacial contact area. In addition, MXene undergoes thermal decomposition under suitable solvothermal conditions, during which the carbon atoms within MXene react with oxygen to form carbon-oxygen bonds. Consequently, MXene is directly converted into CT (Eq. 3), meanwhile, Sr(OH)$_2$ and $Ti(OH)_4$ react with each other and crystallize, forming ST (Eq. 4). Furthermore, in an alkaline solution, the interaction between Sr^{2+} and hydroxide ions (OH$^-$) exhibits weak basicity, which can potentially lead to the partial dissociation of strontium nitrate. This dissociation process releases Sr^{2+} ions and OH$^-$ ions. In addition, the hydrolysis reaction of $Ti(OC_4H_9)_4$ is also reversible, generating some free ions in the reaction solution. These free ions with low concentration will adsorb onto the surface of crystallized ST, promoting the formation of small ST particles. This process reduces surface energy and hinders the ripening of new-nucleated ST. It is worth noting that C-Ti bond in MXene will be broken during the solvothermal process, and bicarbonate will be formed in the solution under alkaline environment, while the free part of Sr^{2+} will be combined with it to generate an extremely small amount of $SrCO_3$ attached to the ST formed at the site (Eq. 5), ultimately yields ST/SC/CT as shown in Fig. 1a. When the mass ratio of MXene to (ST+MXene) is 10%, the sample exhibits the best photocatalytic performance and is denoted as ST/SC/CT unless otherwise stated. The chemical reaction equations involved in the synthesis process are as follows:

$$Sr^{2+} + OH^- + site \rightarrow [Sr(OH)_2]_{ads} \tag{1}$$

$$[Ti(OC_4H_9)_4]_{ads} + 4OH^- \leftrightarrow [Ti(OH)_4]_{ads} + 4 (C_4H_9OH)^- \tag{2}$$

$$Site: MXene \rightarrow C\text{-doped } TiO_2 \tag{3}$$

$$[Sr(OH)_2]_{ads} + [Ti(OH)_4]_{ads} \rightarrow ST + site \tag{4}$$

$$Sr^{2+} + HCO_3^- + OH^- + \rightarrow SrCO_3 + H_2O \tag{5}$$

In Fig. 1b, CT shows that the diffraction peaks at 27.45°, 36.09°, 41.23°, and 54.32°, which belong to (110), (101), (111), and (211) facets of Rutile-TiO_2 (JCPDS No. 21–1276), respectively. Some sharp diffraction peaks in ST are detected at 32.42, 39.98, 46.48, 57.79, 67.80, and 77.18°, which are attributed to the (110), (111), (200), (211), (220), and (310) facets of ST (JCPDS No. 35–0734), respectively. Notably, compared with ST and CT, two new diffraction peaks appear at 25.19° and 25.82° in ST/SC/CT, corresponding to the (111) and (021) facets of SC (JCPDS No. 05–0418).

MXene plays a crucial role in the synthesis of ST/SC/CT. On one hand, MXene serves as the source of CT. Thus, an increase in the mass of MXene in the precursor solution results in a higher amount of CT, leading to an increase in the corresponding peak intensity in the XRD pattern. On the other hand, ST/SC nucleates and grows on the surface of MXene, making MXene the nucleating substrate for ST/SC. As the mass of MXene increases, more ST/SC will grow on the CT surface. Consequently, with an increase in the mass ratio of MXene to (ST+MXene), the XRD peak intensity of ST, SC, and CT increases simultaneously. However, due to the trace amount of SC relative to ST and the coverage of ST/SC on the CT surface, the increase in XRD intensity corresponding to ST is more pronounced (Fig. 1c).

In Figs. S1a-c, ST nanoparticles partly aggregate with the lattice spacing of 0.273 nm. Figs. S1d-e show the sheeted CT. The HRTEM

image in Fig. S1f displays the lattice fringe of 0.338 nm, which is assigned to the (110) crystal plane of CT. Fig. 1d-e show that ST/SC spheres disperse on the surface of CT sheets. This is mainly due to the pinning effect of MXene surface functional groups and the adsorption of low concentration free ions from the precursor solution onto the surface of crystallized ST/SC during the preparation process. The lattice fringes of 0.194, 0.276 and 0.202 nm are attributed to the planes of SC (202), ST (110), and CT (210), respectively (Fig. 1f). Fig. S1g also shows the uniform distribution of Sr, Ti, O, and C elements in ST/SC/CT. Additionally, the specific surface area and pore volume were determined using the Brunauer-Emmett-Teller (BET) theory. Fig. S2 illustrates that the ST/SC/CT exhibits a specific surface area of 55.584 $m^2 \cdot g^{-1}$. It is also evident that the pore distribution and pore volume in ST/SC/CT differ from those in ST and CT, which is attribute to the growth of ST and SC spheres on the surface of CT sheets.

The XPS results of photocatalysts are shown in Fig. 2 and Fig. S3. ST/SC/CT is composed of Sr, O, C, and Ti elements (Fig. S3). Fig. 2a displays the high-resolution XPS spectra of C 1 s for CT and ST/SC/CT. The deconvoluted peaks for ST/SC/CT are located at 288.71 eV, 286.08 eV, 284.80 eV, and 280.98 eV, corresponding to C=O, C-O, C-C, and C-Ti, respectively. Fig. 2b displays the Ti^{4+} $2p_{1/2}$ and Ti^{4+} $2p_{3/2}$ in ST, CT, and ST/SC/CT. Notably, C-Ti bonds (Fig. 2a-b, marked with light orange peaks) are attributed to the C doping into rutile TiO_2 [41]. In Fig. 2c, Sr $3d_{3/2}$ and Sr $3d_{5/2}$ are located at 134.88 eV and 133.12 eV, respectively [42–44]. The spectra of O1s in Fig. 2d shows the lattice oxygen (O_l) and adsorbed oxygen (O_a). Moreover, the electron density will change with binding energy of an element. It means that a decrease in electron density leads to an increase in binding energy. For ST/SC/CT, the Ti 2p, Sr 3d, and O_l peaks shift towards higher binding energy in comparison to ST (Fig. S2b-d), whereas Ti 2p and O_l peaks shift towards lower binding energy in comparison to CT. These shifts indicate changes in the chemical environment or chemical states on the sample surface.

The performance of photocatalytic H_2 production was evaluated using an all-glass automatic on-line trace gas analysis system (Fig. S4). As illustrated in Fig. 3a, ST and CT yield 2.880 mmol g^{-1} and 1.082 mmol g^{-1} of H_2 in three hours, respectively. In contrast, ST/SC/CT generates a remarkable H_2 production of 5.451 mmol g^{-1} during the same period. The according H_2 production activity of ST/SC/CT is 1.817 mmol h^{-1} g^{-1}, which is 1.893 and 5.033 times that of ST and CT under the UV–vis light irradiation, respectively (Fig. 3b). The hydrogen

production activity of ST/SC/CT is higher than that of SC/CT and ST/SC (Fig. S5). This result emphasizes the superiority of ST/SC/CT as a dual S-scheme heterojunction. The apparent quantum efficiency (AQE) values of ST/SC/CT at $\lambda = 365$ nm and $\lambda = 400$ nm are 4.78 % and 0.54 %, respectively, both higher than those of ST and CT.

Besides, the H_2 generation activity of ST/SC/CT is affected by the amounts of MXene during the preparation process. Given that CT is derived from MXene and SC exists in association with ST, variations in the mass of MXene will result in changes in the ratio of ST: SC: and CT. Table S2 demonstrates the effect of the molar ratio of ST: SC: CT on photocatalytic hydrogen production activity. Fig. 3c shows that the optimal mass ratio of MXene to (MXene+ST) is 10 %, resulting in the best sample, ST/SC/CT. However, with a higher mass ratio of MXene/ (ST+MXene), the molar ratio of CT to SC exhibits a decreasing trend, from 8.27 (1.49/0.18) to 2.21 (0.73/0.33), resulting in a corresponding decrease in hydrogen production activity. Thus, only the appropriate molar ratio of ST: SC: CT (1.00: 0.24: 1.16) brought about by the suitable mass ratio of MXene/(ST+MXene) contributes to the improvement of hydrogen production activity.

The H_2 generation activity varies in different sacrificial agent systems (Fig. 3d). In the TEOA system, holes are rapidly consumed due to the low oxidation potentials and high permittivity of TEOA, resulting in the highest hydrogen generation activity compared to other sacrificial agent systems such as lactic acid, methanol, and NaS/Na_2SO_3.

Moreover, ST/SC/CT shows a surface area normalized H_2 generation activity (0.0327 mmol h^{-1} m^{-2}), which is superior to that of ST (0.0175 mmol h^{-1} m^{-2}) and CT (0.0107 mmol h^{-1} m^{-2}). The larger the specific surface area, the more active sites for surface redox reactions. Therefore, the improved H_2 production rate of ST/SC/CT can be partially attributed to its larger surface area (Fig. S2). Additionally, the electrochemical active area (ECSA) was evaluated by characterizing the double layer capacitance (CDL) through multiple cyclic voltammetry tests in the non-Faraday interval (Fig. S6). CDL is positively correlated with ECSA, indicating more abundant catalytic active centers and better photocatalyst activity with higher CDL values. As shown in Fig. 3e, the ECSA normalized H_2 generation activities of ST, CT, and ST/SC/CT are 50.262 mmol cm^2 g^{-1} h^{-1} mF^{-1}, 6.493 mmol cm^2 g^{-1} h^{-1} mF^{-1}, and 89.507 mmol cm^2 g^{-1} h^{-1} mF^{-1}, respectively (The relevant calculation details are presented in the Supporting information). Therefore, the enhanced H_2 production activity of ST/SC/CT can be attributed to both its larger surface area and electrochemical active area. This improves the surface chemical reaction kinetics. Compared with other $SrTiO_3/TiO_2$ photocatalysts, ST/SC/CT shows comparable H_2 production activity under UV–vis light irradiation (Table S3). Additionally, the cycling test of ST/SC/CT shows light loss in photocatalytic H_2 generation after four cycles under UV–vis light irradiation (Fig. 3f). SEM and XRD results display minimal changes in morphology and phase before and after stability testing (Fig. S7). These findings confirm the stability of ST/SC/CT.

The enhancement mechanism of photocatalytic performance was also analyzed in terms of photophysical and electrochemical properties. Fig. S8 shows the optical absorption performance of ST, CT, and ST/SC/CT. ST only absorbs UV light due to its wide bandgap of 3.54 eV [42], whereas CT displays an excellent UV–vis light absorption property as a result of C doping [45]. ST/SC/CT combines the advantages of both ST/SC and CT. On one hand, the visible light absorption range and intensity of ST/SC/CT are significantly improved compared to ST. On the other hand, the UV light absorption intensity of ST/SC/CT is enhanced compared to CT. As a result, ST/SC/CT demonstrates good UV–vis light absorption performance, which plays a crucial role in enhancing photocatalytic performance. As shown in Fig. 3g, the photoluminescence (PL) peak intensity of ST/SC/CT is lower than that of ST and CT, implying the restrained recombination of charge carriers in ST/SC/CT. In addition, electrochemical impedance spectra (EIS) analysis was used to further evaluate the charge transfer property (Fig. 3h). R_{ct} in the equivalent Randle circuit is the interface charge transfer resistance, R_s is
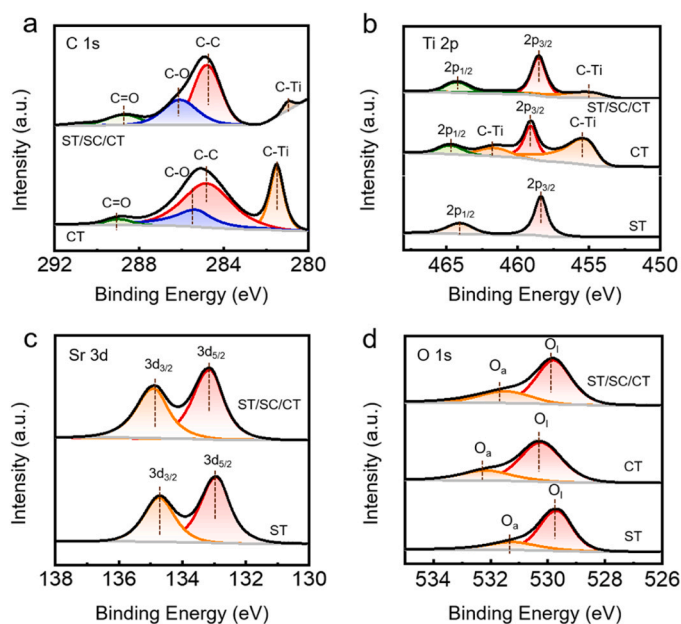

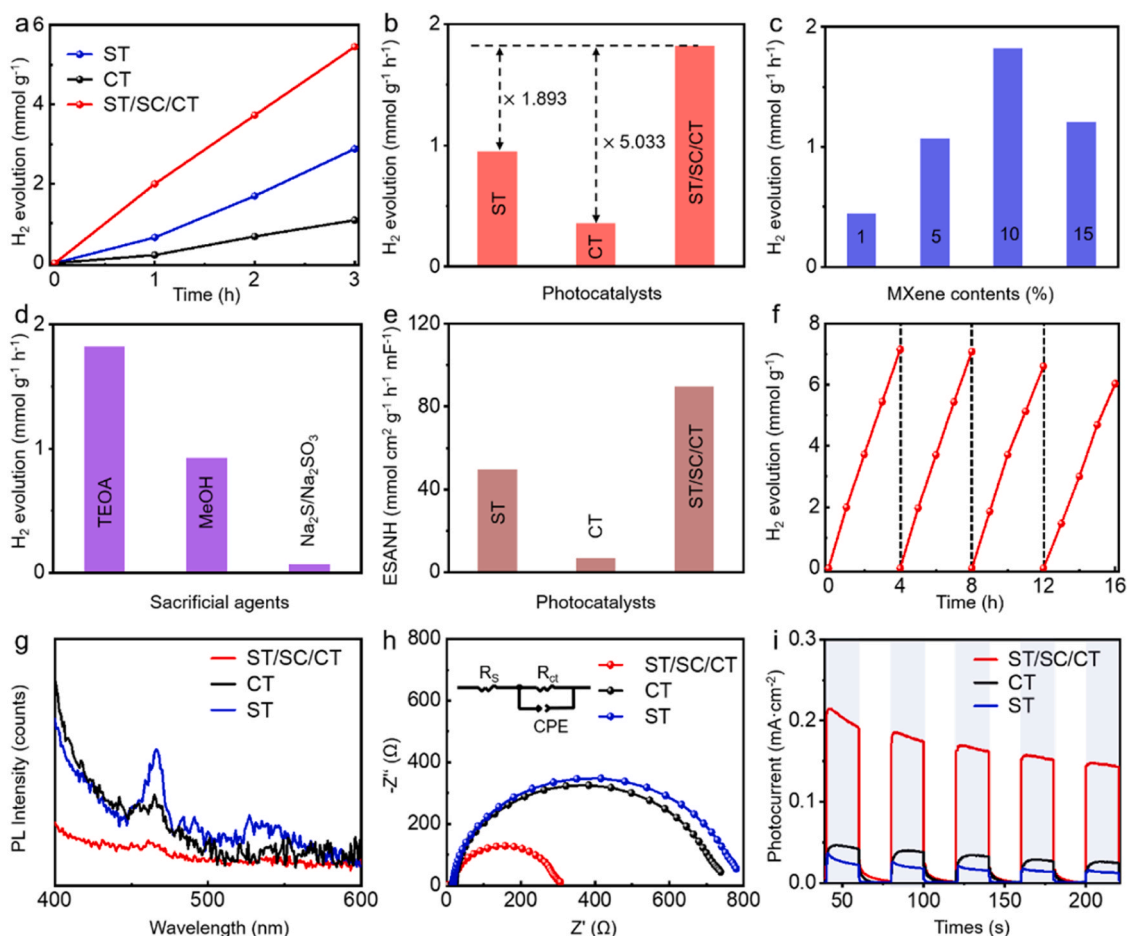**Fig. 2.** XPS spectra of ST, CT, and ST/SC/CT. (a-d) C 1 s, Ti 2p, Sr 3d, and O 1 s spectra, respectively.

Fig. 3. Performance characterization. (a) The time-dependent H$_2$ production curves. (b) H$_2$ production rate of ST, CT, and ST/SC/CT. (c) The influence of mass ratio of MXene to (MXene+ST) on the H$_2$ production activity, respectively. (d) H$_2$ production activity of ST/SC/CT measured in different sacrificial reagent systems. (e) Effective Surface area-normalized H$_2$ evolution activity (ESANH) of ST, CT, and ST/SC/CT. (f) Photocatalytic stability testing of ST/SC/CT. (g) PL spectra. (h) EIS spectra. (i) Transient photocurrent responses of under chopped UV–vis light irradiation. Gray background indicates light on, and white background indicates light off. The photocatalytic reaction was performed under UV–vis irradiation using TEOA as a sacrificial agent.

the electrolyte solution resistance, and CPE is constant phase element (inset in Fig. 3h). ST/SC/CT displays an R$_{ct}$ of 73.6 Ω (Table S4), which is much lower than that of ST (745.7 Ω) and CT (443.6 Ω). Compared with other various samples, the ST/SC/CT possesses the smallest interfacial charge transfer resistance (Fig. S9 and Table S4), which facilitates the charge transfer. Fig. 3i shows the transient photocurrent responses of ST, CT, and ST/SC/CT under chopped UV–vis light irradiation. ST/SC/CT exhibits the highest photocurrent density compared to ST and CT, which is attributed to the enhanced UV–vis light absorption as well as the improved separation and transfer of charge carriers. Additionally, the photocurrent density varies with the mass ratios of MXene to (MXene+ST), as illustrated in Fig. S10.

Therefore, the enhancement of ST/SC/CT photocatalytic activity can be attributed to three factors. Firstly, C doping improved the UV–visible light absorption efficiency of TiO$_2$ (Fig. S8), thereby enhancing the light absorption efficiency of ST/SC/CT. Secondly, the formation of a dual S-scheme heterojunction improved the separation of photogenerated charge carriers. Additionally, a large-area intimate contact interface was constructed using MXene as a medium to enhance the interface charge transfer capability, thereby improving the separation and transfer efficiency of photogenerated charge carriers in ST/SC/CT. Thirdly, a large specific surface area and electrochemical active area contribute to enhancing the surface reaction kinetics of ST/SC/CT in the photocatalytic process. Under the influence of these three factors, ST/SC/CT exhibit good UV–visible light absorption performance, low PL peak intensity, small impedance, and strong photocurrent density.

Consequently, the photocatalytic activity of ST/SC/CT is synergistically enhanced.

The determination of band structure is necessary for the investigation of heterojunction through DFT calculations and experimental verification. The details of DFT calculations are shown in supporting information. The calculated bandgaps of ST, SC, and CS are 3.86, 4.19, and 1.48 eV respectively (Fig. 4a-c). Due to the underestimation of the band gap by the GGA function in VASP and the presence of carbon doping, the calculated band gap of CT will be significantly lower than the results obtained from experiments (Fig. 4h). In Fig. 4d, it can be observed that the VB of ST is mainly contributed by Sr and Ti atoms, while the CB is mainly contributed by O and Ti atoms. For SC, O atoms primarily contribute to the CB, while Sr atoms have significant contributions to the VB, as shown in Fig. 4e. For CT, the CB is mainly composed of C and Ti atoms, while the VB is primarily composed of Ti atoms (Fig. 4f). Therefore, the band structure model obtained by DFT calculations is shown in Fig. S11. Besides the DFT calculations, the band structure model also determined by experiments. As depicted in Fig. 4g, the valence band (VB) values of ST and CT are 1.99 eV and 2.28 eV, respectively, which is collected from valence band X-ray photoelectron spectroscopy (VB-XPS). Then, the E$_{VB}$ of the corresponding standard hydrogen electrode (E$_{VB, NHE}$) can be calculated according to the following formula E$_{VB, NHE}$ = φ+ E$_{VB, XPS}$ -4.44 eV, where φ is the work function of the instrument (4.20 eV). Hence, the E$_{VB, NHE}$ of ST and CT is calculated to be 1.75 eV and 2.04 eV, respectively. In addition, based on the UV–vis DRS spectra using the Taucplot method, the estimated
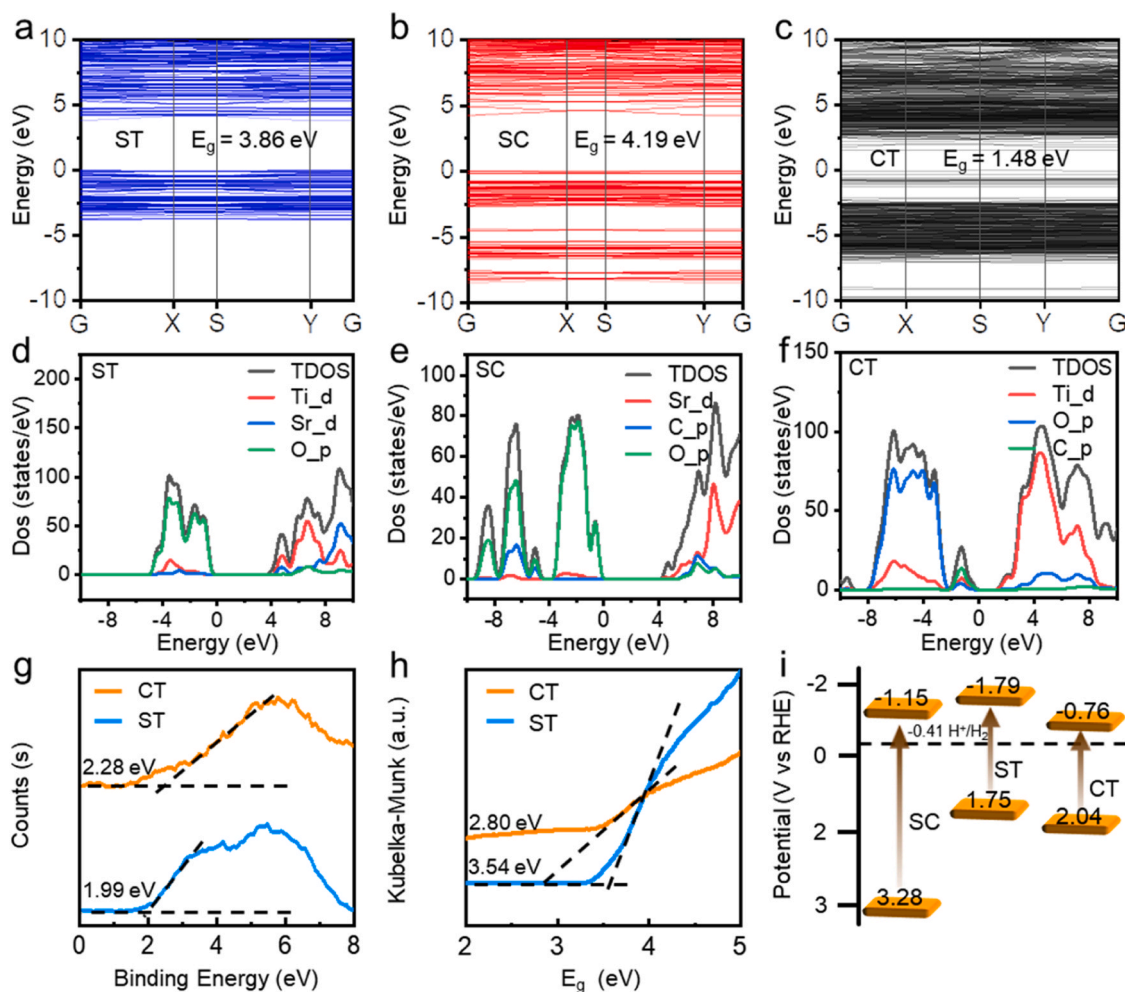
Fig. 4. Band structure of (a) ST, (b) SC, and (c) CT. DOS of (d) ST, (e) SC and (f) CT. (g) VB-XPS spectra of CT and ST; (h) E_g spectra; (i) Band structure diagram.

bandgaps (E_g) for ST and CT are calculated to be 3.54 eV and 2.80 eV (Fig. 4h), respectively. According to the equation of $E_{CB} = E_{VB} - E_g$ (where E_{CB}, E_{VB}, and E_g refer to the conduction band position, valence band position, and bandgap, respectively), the CB positions of ST and CT are determined to be -1.79 eV and -0.76 eV, respectively. In this work, SC generated with ST, so the band structure cannot be directly measured experimentally. According to the data in previous report, the VB and CB positions of SC are at 3.28 eV and -1.15 eV [46]. Therefore, the corresponding band structure alignments of ST, SC, and CT are plotted in Fig. 4i.

Fig. 5 shows the irradiated Kelvin probe force microscopy (KPFM) results. Fig. 5a-c display AFM image, surface potential (SP) mapping under the dark and light conditions, and surface photovoltage (SPV) mapping of ST, CT, and ST/SC/CT, respectively. The SP data are collected using photoirradiation KPFM, and the incident light is a UV–visible spectrum. The contact potential difference (V_{CPD}) is used as the SP value since the same probe was employed in the test (Fig. S12). The difference in SP between dark and light conditions is the surface photovoltage (SPV). Fig. 5a-c show that light irradiation leads to a change in the SP of ST, CT, and ST/SC/CT, indicating that the generation of photogenerated charge carriers caused electron redistribution on the semiconductor surface. In Fig. 5d, the maximum SPV values of ST and CT are 43.33 mV and 25.52 mV, respectively. ST/SC/CT shows complex SPV values compared to ST and CT alone, indicating that the separation and transfer of photogenerated charge carriers differing from those in a single heterojunction.

Based on the band structure and KPFM results (Fig. 4 and Fig. 5), ST/

SC/CT presents multiple charge transfer pathways corresponding to different charge transfer mechanisms, as shown in Fig. S13. Consequently, the charge transfer mechanism in the ST/SC/CT heterojunction was further investigated using DFT calculations. Fig. 6a-c shows the values of work function (Φ) and Fermi level (E_f) for ST, SC, and CT. Specifically, for ST: $\Phi = 3.636$ eV and $E_{f,\ v} = -1.532$ eV; for SC: $\Phi = 4.108$ eV and $E_{f,\ v} = -2.141$ eV; for CT: $\Phi = 4.315$ eV and $E_{f,\ v} = -0.306$ eV. Fig. 6d and e show the results of differential charge density for ST/SC/CT. They reveal that electrons in are transferred ST to SC and CT, resulting in electron accumulation on SC and CT and depletion on ST (Fig. 6d). Near the interface between ST and SC (Fig. 6e), SC becomes negatively charged, while ST is positively charged, attributed to an electrostatic induction. Due to the repulsion between electrons in ST and the negatively charged Helmholtz layer, the potential of ST increases, causing the energy band to bend upward. Conversely, the potential of SC decreases, and the energy band bends downward. Thus, a built-in electrical field (IEF) pointing from ST to SC is established at the interface between ST and SC. Similarly, an IEF pointing from ST to CT is also established at the interface between ST and CT.

Furthermore, the open circuit potential can evaluate the dynamic transport of carriers [47]. In Figs. S14 a, c, e, g, the voltage response of ST/SC/CT under UV–visible light irradiation is high compared to that of ST and CT, indicating that more photogenerated charges are transferred to the electrode, further reflecting the high speed of charge transfer. Transient photocurrent can represent the density of accumulated electrons on the surface [48]. In the electric field formed on the surface of the photocatalyst, electron migration creates an inherent electric field.
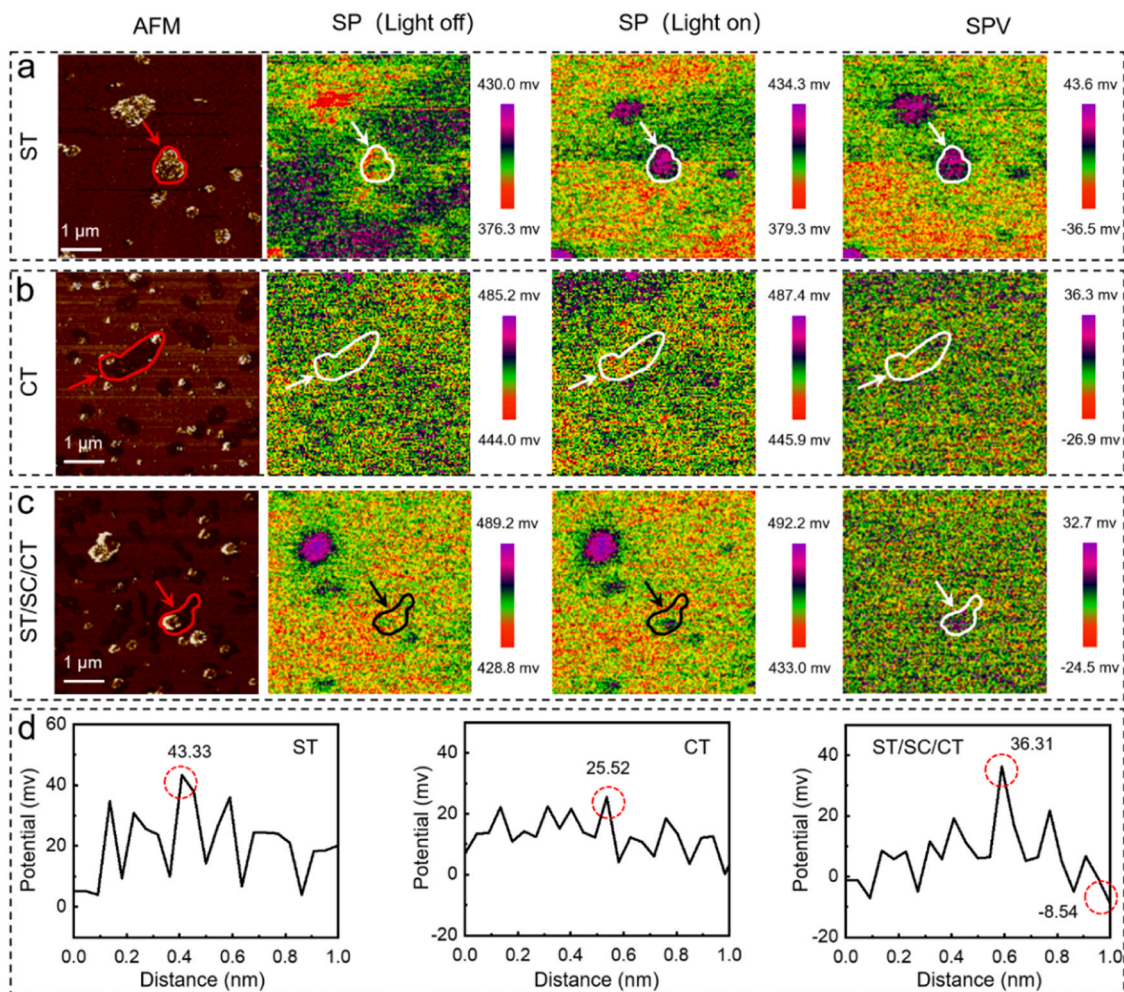
Fig. 5. KPFM characterization of ST, CT, and ST/SC/CT. (a-c) AFM images and the corresponding SP and SPV mappings, respectively. (d-f) SPV line profiles.

The influencing factors are the dynamics of carriers and the density of accumulated electrons on the surface, so the magnitude of the inherent electric field can be quantified through electrochemical measurements [49]. According to Gratzel et al. [50] by subtracting the integral of the measured transient photocurrent density from the steady-state photocurrent as a function of time, the number of charges accumulated by the internal electric field is proportional to the internal electric field intensity. The intensity of IEF in ST/SC/CT is calculated based on an equation [48]:

$$F_s = \left(\frac{-2V_S\rho}{\varepsilon\varepsilon_0} \right)^{\frac{1}{2}}$$

Where F_s, Vs, ε, ε_0, and ρ represent the IEF intensity, surface photovoltage, low frequency dielectric constant, permittivity of free space, and the surface charge density, respectively. Since ε and ε_0 are constants, the magnitude of the IEF intensity can be determined using the surface charge density and the surface photovoltage. The surface charge density is obtained through the integral of the transient anodic photocurrent peak, while the surface voltage is measured via the open-circuit potentials. Therefore, the IEF intensity of different samples can be qualitatively compared according to the $(V_s\rho)^{1/2}$ values from Fig. S14. ST/SC/CT shows the highest photovoltage and charge density, indicating that it has the highest IEF intensity.

A potential dual S-scheme charge transfer ways in ST/SC/CT are illustrated in Fig. 6f. ST, SC, and CT show staggered band positions and Fermi levels. Upon contact between ST, SC, and CT, electrons in ST spontaneously transfer to SC and CT across the interfaces between ST/SC and ST/CT until their Fermi levels align. In this equilibrium state, the energy band of CT and SC are bent downward, while that of ST is bent upward. Two IEFs deviating from ST are established at the interfaces of ST/SC and ST/CT. Under light irradiation, electrons are excited from their VB to CB. Subsequently, the photogenerated electrons in SC and CT combine with holes in ST under the driving force of the IEF. This facilitates efficient charge separation and suppressing charge recombination. Meanwhile, photogenerated electrons with strong reduction ability remain in the CB of ST to reduce H_2O into H_2, while holes with strong oxide ability stay in the VB of SC and CT. Thus, the ST/SC/CT heterojunction follows a dual S-scheme charge transfer mechanism.

4. Conclusion

In summary, we have successfully developed a dual S-scheme ST/SC/CT heterojunction by a simple one-step solvothermal method. Compared to both ST and CT alone, ST/SC/CT exhibits enhanced UV–vis–driven photocatalytic activity. This enhancement is primarily attributed to the dual S-scheme heterojunction, which promotes charge transfer. The potential mechanism is comprehensively investigated through photophysical and electrochemical property analyses, heterojunction characterization, in situ measurements of Kelvin probe force microscopy (KPFM), and density functional theory (DFT) calculations.
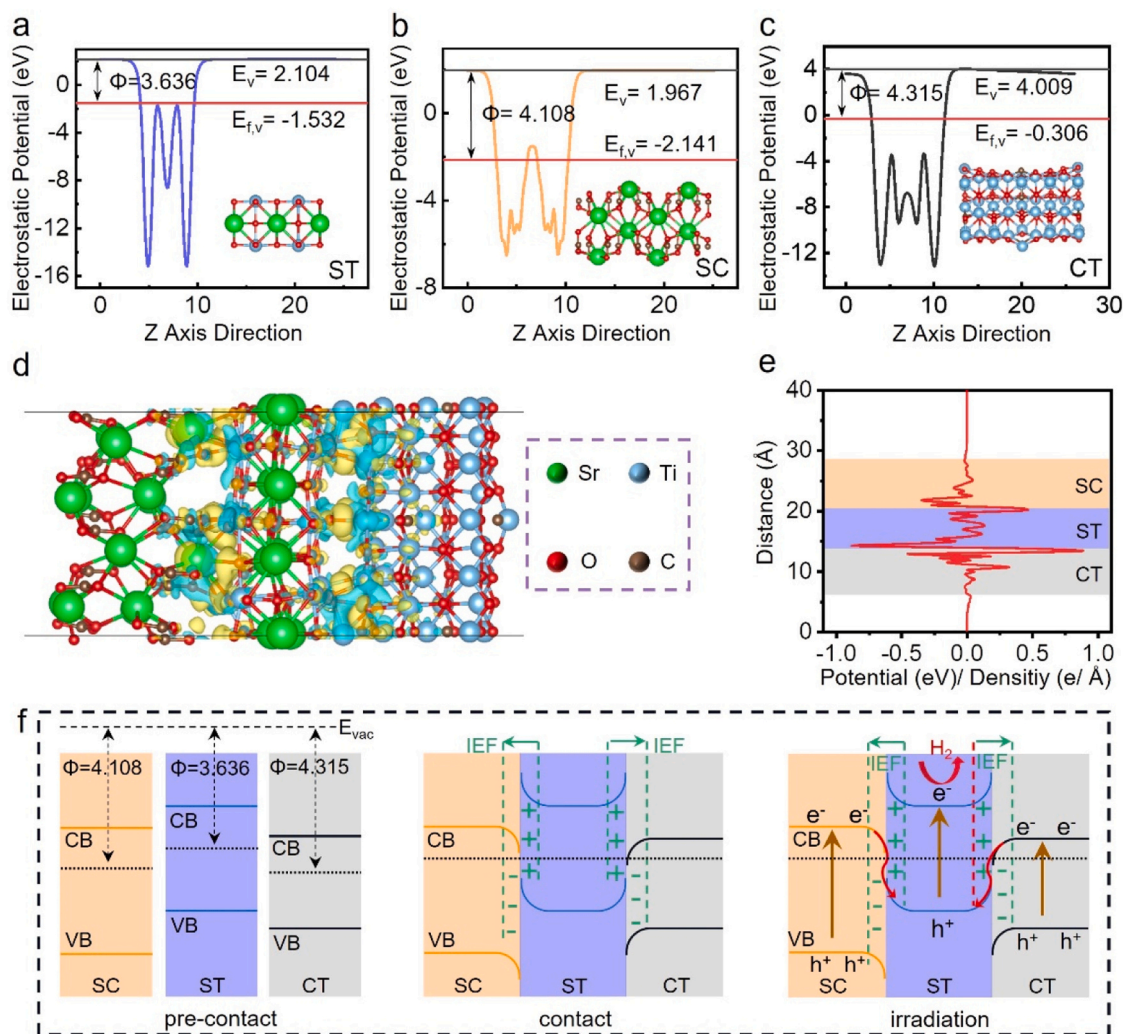
Fig. 6. The possible mechanism. The potential lineup diagrams of (a) ST, (b) SC and (c) CT in ternary material. The illustration represents their respective cellular models.Φ, E_v, and $E_{f,v}$ represent the work function, vacuum energy level, and Fermi energy level under vacuum level, respectively. (d) Differential charge density of ST/SC/CT. Yellow and cyan regions represent the accumulation and loss of electrons, respectively. (e) The charge density difference curve graph of ST/SC/CT. (f) Schematic illustration of dual S-scheme charge carrier transfer process. E_{vac} represents the Vacuum level.

CRediT authorship contribution statement

Qi Hao: Writing – original draft, Methodology, Investigation, Data curation, Conceptualization. **Rongzhong Yang:** Methodology, Investigation, Data curation. **Jing Wang:** Writing – review & editing, Writing – original draft, Supervision, Project administration, Methodology, Investigation, Funding acquisition, Data curation, Conceptualization. **Hui Ying Yang:** Writing – review & editing, Funding acquisition. **Yuping Wu:** Writing – review & editing, Supervision, Investigation, Funding acquisition. **Qinghong Huang:** Writing – review & editing, Validation, Investigation. **Jilei Ye:** Supervision, Funding acquisition. **Liping Yang:** Writing – review & editing, Methodology, Investigation. **Xingyu Niu:** Validation, Methodology, Investigation, Data curation. **Rui Wang:** Methodology, Investigation, Data curation.

Declaration of Competing Interest

The authors declare that they have no known competing financial interests or personal relationships that could have appeared to influence the work reported in this paper.

Data availability

Data will be made available on request.

Acknowledgment

Appendix A. Supporting information

Supplementary data associated with this article can be found in the online version at doi:10.1016/j.apcatb.2024.124232.

References

[1] A. Fujishima, K. Honda, Electrochemical photolysis of water at a semiconductor electrode, Nature 238 (1972) 37–38, https://doi.org/10.1038/238037a0.

[2] Y. Yang, L.C. Yin, Y. Gong, P. Niu, J.Q. Wang, L. Gu, X. Chen, G. Liu, L. Wang, H. M. Cheng, An unusual strong visible-light absorption band in red anatase TiO$_2$ photocatalyst induced by atomic hydrogen-occupied oxygen vacancies, Adv. Mater. 30 (2018) 1704479, https://doi.org/10.1002/adma.201704479.

[3] S. Li, Y.H. Ng, R. Zhu, S. Lv, C. Wu, Y. Liu, L. Jing, J. Deng, H. Dai, In situ construction of elemental phosphorus nanorod-modified TiO$_2$ photocatalysts for efficient visible-light-driven H$_2$ generation, Appl. Catal. B Environ. 297 (2021) 120412, https://doi.org/10.1016/j.apcatb.2021.120412.

[4] Y. Li, H. Zhou, S. Cai, D. Prabhakaran, W. Niu, A. Large, G. Held, R.A. Taylor, X.-P. Wu, S.C.E. Tsang, Electrolyte-assisted polarization leading to enhanced charge separation and solar-to-hydrogen conversion efficiency of seawater splitting, Nat. Catal. 7 (2024) 77–88, https://doi.org/10.1038/s41929-023-01069-1.

[5] Z. Li, Z. Sun, G. Zhang, Combining heterogeneous photocatalysis and enzymatic catalysis via membrane: conversion of biomass for H$_2$ production from water, Appl. Catal. B Environ. 338 (2023) 123069, https://doi.org/10.1016/j.apcatb.2023.123069.

[6] J. Zhang, Y. Pan, D. Feng, L. Cui, S. Zhao, J. Hu, S. Wang, Y. Qin, Mechanistic insight into the synergy between platinum single atom and cluster dual active sites boosting photocatalytic hydrogen evolution, Adv. Mater. 35 (2023) 2300902, https://doi.org/10.1002/adma.202300902.

[7] Y. Zhang, W. Zhou, L. Jia, X. Tan, Y. Chen, Q. Huang, B. Shao, T. Yu, Visible light driven hydrogen evolution using external and confined CdS: effect of chitosan on carriers separation, Appl. Catal. B Environ. 277 (2020) 119152, https://doi.org/10.1016/j.apcatb.2020.119152.

[8] S. Chattopadhyay, A.B. Naden, W.S.J. Skinner, G. Kerherve, D.J. Payne, J.T. S. Irvine, Room temperature exsolution of Cds nanodots on A-site deficient cotton-ball like titanate perovskite nanoparticles for H$_2$ production under visible light, Adv. Energy Mater. 13 (2023) 2301381, https://doi.org/10.1002/aenm.202301381.

[9] X. Zheng, Y. Song, Y. Liu, Y. Yang, D. Wu, Y. Yang, S. Feng, J. Li, W. Liu, Y. Shen, X. Tian, ZnIn$_2$S$_4$-based photocatalysts for photocatalytic hydrogen evolution via water splitting, Coord. Chem. Rev. 475 (2023) 214898, https://doi.org/10.1016/j.ccr.2022.214898.

[10] Y. Guo, J. Sun, Y. Tang, X. Jia, Y. Nie, Z. Geng, C. Wang, J. Zhang, X. Tan, D. Zhong, J. Ye, T. Yu, Efficient interfacial electrons transfer induced by hollow-structured ZnIn$_2$S$_4$ extending hot electrons lifetimes, Energy Environ. Sci. 16 (2023) 3462–3473, https://doi.org/10.1039/d3ee01522j.

[11] Y. Su, Z. Wei, Y. Lian, Q. Mu, W. Pan, D. Song, Y. Qin, W. Hua, J. Cheng, Z. Deng, Y. Peng, Defect-driven electroless deposition and activation of platinum sites on ZnIn$_2$S$_4$ nanosheets for accelerated kinetics of photocatalytic hydrogen production, Appl. Catal. B Environ. 334 (2023) 122827, https://doi.org/10.1016/j.apcatb.2023.122827.

[12] Q. Wang, S. Okunaka, H. Tokudome, T. Hisatomi, M. Nakabayashi, N. Shibata, T. Yamada, K. Domen, Printable photocatalyst sheets incorporating a transparent conductive mediator for Z-scheme water splitting, Joule 2 (2018) 2667–2680, https://doi.org/10.1016/j.joule.2018.08.003.

[13] Z. Zhao, R.V. Goncalves, S.K. Barman, E.J. Willard, E. Byle, R. Perry, Z. Wu, M. N. Huda, A.J. Moulé, F.E. Osterloh, Electronic structure basis for enhanced overall water splitting photocatalysis with aluminum doped SrTiO$_3$ in natural sunlight, Energy Environ. Sci. 12 (2019) 1385–1395, https://doi.org/10.1039/c9ee00310j.

[14] B. Moss, Q. Wang, K.T. Butler, R. Grau-Crespo, S. Selim, A. Regoutz, T. Hisatomi, R. Godin, D.J. Payne, A. Kafizas, K. Domen, L. Steier, J.R. Durrant, Linking in situ charge accumulation to electronic structure in doped SrTiO$_3$ reveals design principles for hydrogen-evolving photocatalysts, Nat. Mater. 20 (2021) 511–517, https://doi.org/10.1038/s41563-020-00868-2.

[15] C. Avcıoğlu, S. Avcıoğlu, M.F. Bekheet, A. Gurlo, Photocatalytic overall water splitting by SrTiO$_3$: progress report and design strategies, ACS Appl. Energy Mater. 6 (2023) 1134–1154, https://doi.org/10.1021/acsaem.2c03280.

[16] B. Moss, Q. Wang, K.T. Butler, R. Grau-Crespo, S. Selim, A. Regoutz, T. Hisatomi, R. Godin, D.J. Payne, A. Kafizas, K. Domen, L. Steier, J.R. Durrant, Linking in situ charge accumulation to electronic structure in doped SrTiO$_3$ reveals design principles for hydrogen evolving photocatalysts, Nat. Mater. 20 (4) (2021) 511–517, https://doi.org/10.1038/s41563-020-00868-2.

[17] A. Hossain, T.C. Bhagya, E.A. Mukhanova, A.V. Soldatov, A.M.A. Henaish, Y. Mao, S.M.A. Shibli, Engineering strontium titanate-based photocatalysts for green hydrogen generation: recent advances and achievements, Appl. Catal. B Environ. 342 (2024) 123383, https://doi.org/10.1016/j.apcatb.2023.123383.

[18] A. Dhakshinamoorthy, Z. Li, S. Yang, H. Garcia, Metal–organic framework heterojunctions for photocatalysis, Chem. Soc. Rev. 53 (2024) 3002–3035, https://doi.org/10.1039/D3CS00205E.

[19] H. Wen, W. Duan, L. Guo, Q. Wang, X. Fu, Y. Wang, R. Li, B. Jin, R. Du, C. Yang, D. Wang, Directing charge transfer in a chemical-bonded Ni/Cd$_{0.7}$Mn$_{0.3}$S Schottky heterojunction for selective photocatalytic oxidation of benzyl alcohol structural organic platform molecules coupled with hydrogen evolution reaction, Appl. Catal. B Environ. 345 (2024) 123641, https://doi.org/10.1016/j.apcatb.2023.123641.

[20] U. Sahoo, S. Pattnayak, S. Choudhury, P. Aparajita, D.K. Pradhan, G. Hota, Facile synthesis of defect induced CeO$_2$/MIL-53(Fe) nanocatalyst: strategically switching the charge transfer dynamics for remarkable enhancement of photocatalytic bisphenol A degradation and H$_2$ evolution, Appl. Catal. B Environ. 343 (2024) 123524, https://doi.org/10.1016/j.apcatb.2023.123524.

[21] Y. He, L. Zhang, Y. Wei, X. Chang, Z. Wang, R. Yu, Semicrystalline SrTiO$_3$-decorated anatase TiO$_2$ nanopie as heterostructure for efficient photocatalytic hydrogen evolution, Small Methods 6 (2022) 2101567, https://doi.org/10.1002/smtd.202101567.

[22] K. Song, H. Hou, D. Zhang, F. He, W. Yang, In-situ cation-exchange strategy for engineering single-atomic Co on TiO$_2$ photoanode toward efficient and durable

[23] solar water splitting, Appl. Catal. B Environ. 330 (2023) 122630, https://doi.org/10.1016/j.apcatb.2023.122630.

[23] D. Gao, P. Deng, J. Zhang, L. Zhang, X. Wang, H. Yu, J. Yu, Reversing free-electron transfer of MoS$_{2+x}$ cocatalyst for optimizing antibonding-orbital occupancy enables high photocatalytic H$_2$ evolution, Angew. Chem. Int. Ed. 62 (2023) e202304559, https://doi.org/10.1002/anie.202304559.

[24] D. Gao, H. Long, X. Wang, J. Yu, H. Yu, Tailoring antibonding-orbital occupancy state of selenium in Se-enriched ReSe$_{2+x}$ cocatalyst for exceptional H$_2$ evolution of TiO$_2$ photocatalyst, Adv. Funct. Mater. 33 (2023) 2209994, https://doi.org/10.1002/adfm.202209994.

[25] A. Piątkowska, M. Janus, K. Szymański, S. Mozia, C-,N- and S-doped TiO$_2$ photocatalysts: a review, Catalysts 11 (2021) 144, https://doi.org/10.3390/catal11010144.

[26] S. Chen, Y.H. Hu, Color TiO$_2$ materials as emerging catalysts for visible-NIR light photocatalysis, a review, Catal. Rev. (2023) 1–41, https://doi.org/10.1080/01614940.2023.2169451.

[27] W. Wang, S. Mei, H. Jiang, L. Wang, H. Tang, Q. Liu, Recent advances in TiO$_2$-based S-scheme heterojunction photocatalysts, Chin. J. Catal. 55 (2023) 137–158, https://doi.org/10.1016/S1872-2067(23)64551-6.

[28] B. Li, W. Peng, J. Zhang, J.C. Lian, T. Huang, N. Cheng, Z. Luo, W.Q. Huang, W. Hu, A. Pan, High-throughput one-photon excitation pathway in 0D/3D heterojunctions for visible-light driven hydrogen evolution, Adv. Funct. Mater. 31 (2021) 2100816, https://doi.org/10.1002/adfm.202100816.

[29] B. Li, Z. Tian, L. Li, Y.-H. Wang, Y. Si, H. Wan, J. Shi, G.-F. Huang, W. Hu, A. Pan, Directional charge transfer channels in a monolithically integrated electrode for photoassisted overall water splitting, ACS Nano 17 (2023) 3465–3482, https://doi.org/10.1021/acsnano.2c09659.

[30] W. Wang, S. Mei, H. Jiang, L. Wang, H. Tang, Q. Liu, Recent advances in TiO$_2$-based S-scheme heterojunction photocatalysts, Chin. J. Catal. 55 (2023) 137–158, https://doi.org/10.1016/S1872-2067(23)64551-6.

[31] L. Zhang, J. Zhang, H. Yu, J. Yu, Emerging S-scheme photocatalyst, Adv. Mater. 34 (2022) 2107668, https://doi.org/10.1002/adma.202107668.

[32] X. Wang, Z. Jin, Adjusting inter-semiconductor barrier height via crystal plane engineering: Crystalline face exposed single crystal cadmium sulfide augmentative S-scheme heterojunctions for efficiently photocatalytic hydrogen production, Appl. Catal. B Environ. 342 (2024) 123373, https://doi.org/10.1016/j.apcatb.2023.123373.

[33] Y. Zhong, M. Li, X. Luan, F. Gao, H. Wu, J. Zi, Z. Lian, Ultrathin ZnIn$_2$S$_4$/ZnSe heteronanosheets with modulated S-scheme enable high efficiency of visible-light-responsive photocatalytic hydrogen evolution, Appl. Catal. B Environ. 335 (2023) 122859, https://doi.org/10.1016/j.apcatb.2023.122859.

[34] Y. Xiao, M. Li, H. Li, Z. Wang, Y. Wang, Multi-channel charge transfer in self-supporting B-g-C$_3$N$_x$/Bi$_2$S$_3$/CdS dual S-scheme heterojunction toward enhanced photothermal-photocatalytic performance, Nano Energy 120 (2024) 109164, https://doi.org/10.1016/j.nanoen.2023.109164.

[35] X. Luan, Z. Yu, J. Zi, F. Gao, Z. Lian, Photogenerated defect-transit dual S-scheme charge separation for highly efficient hydrogen production, Adv. Funct. Mater. 33 (2023) 2304259, https://doi.org/10.1002/adfm.202304259.

[36] C. Chang, H. Lu, Y. Liu, G. Long, X. Guo, X. Ji, Z. Jin, Novel CoV-LDH/GDY/CuI tandem double S-scheme heterojunction based on graphdiyne (g-C$_n$H$_{2n-2}$) toward photocatalytic hydrogen evolution, J. Mater. Chem. A 12 (2024) 4204–4220, https://doi.org/10.1039/d3ta06906k.

[37] J.P. Perdew, K. Burke, M. Ernzerhof, Generalized gradient approximation made simple, Phys. Rev. Lett. 77 (18) (1996) 3865–3868, https://doi.org/10.1103/PhysRevLett.77.3865.

[38] G. Kresse, D. Joubert, From ultrasoft pseudopotentials to the projector augmented-wave method, Phys. Rev. B 59 (1999) 1758–1775, https://doi.org/10.1103/PhysRevB.59.1758.

[39] S. Grimme, J. Antony, S. Ehrlich, H. Krieg, A consistent and accurate ab initio parametrization of density functional dispersion correction (DFT-D) for the 94 elements H-Pu, J. Chem. Phys. 132 (2010), https://doi.org/10.1063/1.3382344.

[40] H.J. Monkhorst, J.D. Pack, Special points for Brillouin-zone integrations, Phys. Rev. B 13 (1976) 5188–5192, https://doi.org/10.1103/PhysRevB.13.5188.

[41] Y. Park, W. Kim, H. Park, T. Tachikawa, T. Majima, W. Choi, Carbon-doped TiO$_2$ photocatalyst synthesized without using an external carbon precursor and the visible light activity, Appl. Catal. B Environ. 91 (2009) 355–361, https://doi.org/10.1016/j.apcatb.2009.06.001.

[42] W. Zhang, Y. Li, L. Wang, F. Zhang, Y. Ai, G. Shao, P. Zhang, In situ construction of cyano-modified g-C$_3$N$_4$ nanolayer-coated SrTiO$_3$ nanotubes by gas-solid reaction for efficient photocatalytic solar fuel production, Chem. Eng. J. 469 (2023) 143817, https://doi.org/10.1016/j.cej.2023.143817.

[43] Y. Zhang, C. Liu, Y. Zhou, J. Wang, A. Li, P.F.-X. Corvini, Boosting light harvesting and charge separation over hollow double-shelled Ag@SrTiO$_3$-TiO$_2$ with Z-scheme heterostructure for highly efficient photocatalytic reduction of nitrate to N$_2$, Chem. Eng. J. 457 (2023) 140992, https://doi.org/10.1016/j.cej.2022.140992.

[44] J. Wang, M. Kuo, P. Zeng, L. Xu, S. Chen, T. Peng, Few-layer BiVO$_4$ nanosheets decorated with SrTiO$_3$: Rh nanoparticles for highly efficient visible-light-driven overall water splitting, Appl. Catal. B Environ. 279 (2020) 119377, https://doi.org/10.1016/j.apcatb.2020.119377.

[45] S.-M. Huang, C.-H. Weng, J.-H. Tzeng, Y.-Z. Huang, J. Anotai, L.-T. Yen, C.-J. Chang, Y.-T. Lin, Photocatalytic inactivation of Klebsiella pneumoniae by visible-light-responsive N/C-doped and N-tourmaline/palladium-C-codoped TiO$_2$, Chem. Eng. J. 379 (2020) 122345, https://doi.org/10.1016/j.cej.2019.122345.

[46] H. Wang, Y. Sun, G. Jiang, Y. Zhang, H. Huang, Z. Wu, S.C. Lee, F. Dong, Unraveling the mechanisms of visible light photocatalytic NO purification on

earth-abundant insulator-based core-shell heterojunctions, Environ. Sci. Technol. 52 (2018) 1479–1487, https://doi.org/10.1021/acs.est.7b05457.

[47] L. Xia, Z. Sun, Y. Wu, X.-F. Yu, J. Cheng, K. Zhang, S. Sarina, H.-Y. Zhu, H. Weerathunga, L. Zhang, Leveraging doping and defect engineering to modulate exciton dissociation in graphitic carbon nitride for photocatalytic elimination of marine oil spill, Chem. Eng. J. 439 (2022) 135668, https://doi.org/10.1016/j.cej.2022.135668.

[48] Y. Zhang, Y. Li, X. Xin, Y. Wang, P. Guo, R. Wang, B. Wang, W. Huang, A. J. Sobrido, X. Li, Internal quantum efficiency higher than 100% achieved by combining doping and quantum effects for photocatalytic overall water splitting, Nat. Energy 8 (2023) 504–514, https://doi.org/10.1038/s41560-023-01242-7.

[49] Peipei Sun, Jinyuan Zhang, Yanhua Song, Zhao Mo, Zhigang Chen, Hui Xu, Built-in electric fields enhancing photocarrier separation and H$_2$ evolution, Acta Phys. -Chim. Sin. (2023) 2311001, https://doi.org/10.3866/PKU.WHXB202311001.

[50] F. Le Formal, K. Sivula, M. Grätzel, The transient photocurrent and photovoltage behavior of a hematite photoanode under working conditions and the influence of surface treatments, J. Phys. Chem. C 116 (2012) 26707–26720, https://doi.org/10.1021/jp308591k.